Smart Grid and Renewable Energy, 2026, 17(8), 197-222
https://www.scirp.org/journal/sgre
ISSN Online: 2151-4844
ISSN Print: 2151-481X

Resilience and Energy Optimization of Grid-Connected PV Systems during Disruptions

Armel Duvalier Pene[1*], Kitmo[2], Lucian Toma[3], Noël Djongyang[2]

[1]Department of Electrical Engineering, University Institute of Technology, University of Ngaoundéré, Ngaoundéré, Cameroon
[2]Department of Renewable Energy, National Advanced School of Engineering of Maroua, University of Maroua, Maroua, Cameroon
[3]Faculty of Energy Engineering, National University of Science and Technology POLITEHNICA Bucharest, Bucharest, Romania
Email: *duvalierarmel@gmail.com

How to cite this paper: Pene, A.D., Kitmo, Toma, L. and Djongyang, N. (2026) Resilience and Energy Optimization of Grid-Connected PV Systems during Disruptions. *Smart Grid and Renewable Energy*, **17**, 197-222.
https://doi.org/10.4236/sgre.2026.178010

Received: May 20, 2026
Accepted: July 31, 2026
Published: August 19, 2026

Abstract

Modern microgrids have significant challenges in terms of stability and power quality when intermittent renewable energy sources, particularly solar photovoltaics, are integrated. In order to overcome this, we offer a strong framework for energy management and optimization that is intended for grid-connected hybrid (PV-Battery) systems that are subjected to significant disruptions. The main innovation is a Battery Energy Storage System (BESS) powered by a dynamic power-smoothing algorithm that actively counteracts both local demand spikes and abrupt reductions in solar irradiation. The system effectively controls frequency and preserves voltage stability at the Point of Common Coupling (PCC) by using a real-time control approach. Numerical models that replicate important events, such as grid failures and sudden weather changes, were used to verify the arrangement. According to the statistics, our approach effectively reduces peak demands while maintaining high power quality and securely keeping the Total Harmonic Distortion (THD) within the IEEE 1547 standard's 5% limit. In the end, our approach offers a workable way to construct more resilient grids during the current energy transition.

Keywords

Power Smoothing, Frequency Stability, Power Quality, Microgrid, Battery Energy Storage System (BESS), Real-Time Optimization

1. Introduction

The contribution of solar energy to the world's energy mix has changed throughout three different stages [1], moving from passive generation to intelligent, robust management [2]. Photovoltaic systems functioned simply as fundamental power sources in the early stages of this shift, with the sole purpose of directly injecting their whole output into the public grid [3]. These early installations were characterized by certain limitations and principles of operation. For example, the inverter only synchronized its output with the voltage and frequency set by the main grid, operating strictly in a "grid-following" mode [4]. A significant disadvantage of this configuration was that anti-islanding protection required an instantaneous system shutdown for safety in the event of a main grid failure. As a result, even in direct sunlight, local customers were left without solar electricity [5].

1.1. Increase in Storage and Self-Consumption

Technology has changed to maximize self-consumption due to declining battery prices and shifting restrictions [6]. Technological aspect: The introduction of hybrid inverters that can control a battery bank, a PV array, and the grid connection all at once. Contribution aspect: Although management was frequently restricted to a single building without dynamic interaction with external disturbances, this step made it feasible to smooth PV output and lessen reliance on the grid.

1.2. Development of Intelligent Microgrids

The age of smart microgrids is upon us [7]. A microgrid is a local energy system that may function independently (in island mode) or as a part of a larger network. Intelligent embedded systems: Monitoring algorithms (Energy Management Systems, or EMS) that employ artificial intelligence for energy arbitrage are included into current technology. Advanced control: Enter "Grid-forming" mode, in which the power electronics may produce and sustain grid characteristics (frequency and voltage) even when the primary power source is not present [8]. Resilience to disruptions: In contrast to earlier systems, the contemporary microgrid uses grid support functions (ancillary services) to proactively handle disruptions (voltage drops, frequency fluctuations), guaranteeing ideal service continuity [9].

2. Integration of Novel Approach

The majority of traditional energy management techniques (EMS) are restricted on minimizing an economic cost function C_{total}, which is commonly described as [10].

$$\min \int_0^T \left(C_{\text{achat}} \cdot P_{\text{grid}}(t) + C_{\text{om}} \cdot P_{\text{pv}}(t) + C_{\text{deg}} \cdot P_{\text{batt}}(t) \right) \mathrm{d}t \tag{1}$$

where, P_{grid}, P_{pv} et P_{batt} respectively, stand for the electricity from the grid, the solar array, and the batteries. Nevertheless, fast dynamics during disturbances are not taken into consideration by this method. The originality of our method consists in the inclusion of dynamic resilience directly into the optimization algorithm [11].

Our method is unusual because it incorporates dynamic resilience right into the optimization technique.

3. Multi-Objective Objective Function Formulation

We provide a hybrid cost function that weighs stability performance metrics and economic variables in contrast to conventional methods [12]:

$$J = \alpha \cdot C_{\text{economique}} + \beta \cdot \Phi_{\text{stabilite}} \tag{2}$$

where $\Phi_{\text{stability}}$ is a penalty term associated with variations in voltage and frequency [13]:

$$\Phi_{\text{stabilite}} = \int_0^T \left[\left(\frac{V_{\text{pcc}}(t) - V_{\text{ref}}}{V_{\text{ref}}} \right)^2 + \left(\frac{f(t) - f_{\text{ref}}}{f_{\text{ref}}} \right)^2 \right] \text{d}t \tag{3}$$

3.1. Using Stability Restrictions When There Are Disruptions

The difference is that the constraints now incorporate differential constraints related to the dynamics of the system during disturbances in addition to algebraic constraints (power balances).

In order to rigorously define the Model Predictive Control (MPC) framework, the control strategy evaluates future system behavior over a finite prediction horizon N_{p} and calculates the optimal control sequence over a control horizon N_{c}. In this study, the prediction horizon is set to $N_{\text{p}} = 10$ steps, and the control horizon is set to $N_{\text{c}} = 3$ steps, striking an optimal balance between dynamic performance and computational burden.

The state vector $x(k)$ of the MPC model integrates the battery power, the State of Charge (SOC), and the DC-link voltage. The control input vector $u(k)$ represents the reference signals sent to the power converters. At each sampling instant k (with $T_{\text{s}} = 1\,\text{ms}$), the multi-objective cost function J is formulated to minimize tracking errors while respecting physical and operational constraints [14]:

$$\begin{aligned} J = \sum_{j=1}^{N_p} \Big[& w_1 \left(P_{\text{grid}}^*(k+j|k) - P_{\text{grid}}(k+j|k) \right)^2 \\ & + w_2 \left(V_{\text{dc}}^*(k+j|k) - V_{\text{dc}}(k+j|k) \right)^2 + w_3 \left(\Delta u(k+j-1) \right)^2 \Big] \end{aligned} \tag{4}$$

where w_1, w_2, and w_3 are weighting factors prioritizing power smoothing, DC-link voltage stability, and control effort minimization, respectively.

The optimization problem is subject to the following hard and soft constraints [15]:

- **Power limits:** $-P_{\text{batt,max}} \le P_{\text{batt}}(k+j|k) \le P_{\text{batt,max}}$.
- **SOC limits:** $\text{SOC}_{\min} \le \text{SOC}(k+j|k) \le \text{SOC}_{\max}$.
- **DC-link voltage limits:** $0.9V_{\text{dc,nom}} \le V_{\text{dc}}(k+j|k) \le 1.1V_{\text{dc,nom}}$.

The resulting constrained optimization problem is mapped into a standard

Quadratic Programming (QP) problem and solved efficiently at every sampling step using an active-set solver implemented within MATLAB [16].

3.2. Smoothing Out Variations

We simulate inertia by imposing a restriction on the derivative of the injected power in order to counteract abrupt changes in sunlight ΔP_{pv} [17]:

$$P_{\text{batt}}(t) = P_{\text{load}}(t) - P_{\text{pv}}(t) - J_{\text{virt}} \cdot \omega_0 \frac{\mathrm{d}\Delta f}{\mathrm{d}t} \tag{5}$$

where J_{virt} is the virtual moment of inertia introduced by the storage system [18].

3.3. The DC Bus's Resilience Limitations

The DC bus voltage V_{dc} may fluctuate in the case of a power outage (voltage drop). Our method places a stringent safety restriction on [19]:

$$V_{\text{dc,min}} \le \sqrt{\frac{2}{C}\int \left(P_{\text{pv}} + P_{\text{batt}} - P_{\text{inv}}\right)\mathrm{d}t} \le V_{\text{dc,max}} \tag{6}$$

4. Predictive Control System

The suggested method anticipates interruptions by using a prediction horizon. The method resolves the following issue at each time step k [20]:

$$\min_u \sum_{i=k}^{k+N} \left\| \hat{y}(i) - y_{\text{ref}} \right\|_Q^2 + \left\| \Delta u(i) \right\|_R^2 \tag{7}$$

$$\text{As: } \begin{cases} x(i+1) = Ax(i) + Bu(i) + Dd(i) \\ V_{\min} \le V(i) \le V_{\max} \\ f_{\min} \le f(i) \le f_{\max} \end{cases} \tag{8}$$

where $d(i)$ represents the disturbance vector (irradiation, load, grid faults).

The technique described here guarantees that the state variables (V, f) remain within stringent safety limits even in degraded mode (severe disruptions) owing to proactive management of the batteries' power reserve, whereas conventional approaches occasionally sacrifice energy quality in order to cut costs [21].

5. System Modelling

A set of linked equations that describe the solar source, storage system, and converter interface are used to model the hybrid microgrid [22].

5.1. Modelling of the Photovoltaic (PV) Generator

Temperature and irradiance affect the PV array's output power. The connection serves as a model [23]:

$$P_{\text{pv}} = \eta_{\text{pv}} \cdot S_{\text{pv}} \cdot G \cdot \left[1 - 0.005\left(T_{\text{cell}} - 25\right)\right] \tag{9}$$

where:

- G: Irradiation (W/m^2).

- S_{pv} : Total panel area.
- η_{pv} : nominal efficiency.

5.2. DC-Link Dynamics

The main element where power flows converge is the DC bus. The rule of conservation of energy stored in the capacitance controls its behavior C_{dc} [24]:

$$C_{\mathrm{dc}} V_{\mathrm{dc}} \frac{\mathrm{d}V_{\mathrm{dc}}}{\mathrm{d}t} = P_{\mathrm{pv}} \pm P_{\mathrm{batt}} - P_{\mathrm{inv}} \tag{10}$$

where P_{inv} is the power transferred to the inverter.

5.3. Modeling the Voltage-Source Inverter (VSI)

In order to separate the active power (P) and reactive power (Q), the grid-connected inverter is modeled in the synchronous reference frame [25]:

$$\begin{cases} P = \frac{3}{2}\left(v_{\mathrm{d}} i_{\mathrm{d}} + v_{\mathrm{q}} i_{\mathrm{q}}\right) \\ Q = \frac{3}{2}\left(v_{\mathrm{q}} i_{\mathrm{d}} - v_{\mathrm{d}} i_{\mathrm{q}}\right) \end{cases} \tag{11}$$

If the reference point is aligned with the mains voltage ($v_{\mathrm{q}} = 0$), the equations become simpler [26]:

$$\begin{cases} P = \frac{3}{2} v_{\mathrm{d}} i_{\mathrm{d}} \\ Q = -\frac{3}{2} v_{\mathrm{d}} i_{\mathrm{q}} \end{cases} \tag{12}$$

5.4. State Equations of the Output Filter (LCL)

We simulate the coupling filter between the inverter and the point of connection (PCC) in order to analyze stability in the presence of disruptions [27]:

$$L \frac{\mathrm{d}i_{\mathrm{inv}}}{\mathrm{d}t} = V_{\mathrm{inv}} - V_{\mathrm{pcc}} - R i_{\mathrm{inv}} \tag{13}$$

5.5. Load Model and Overall Balance

When there are network disruptions, the power balance at the common coupling point (CCP) is determined by [28]:

$$P_{\mathrm{grid}} = P_{\mathrm{load}} - \left(P_{\mathrm{pv}} + P_{\mathrm{batt}} - P_{\mathrm{loss}}\right) \tag{14}$$

6. Battery Energy Storage System

To prevent any ambiguity in the interpretation of the BESS operation and its impact on the microgrid energy balance, a strict and consistent sign convention is established throughout this paper and across all figures [29]:

Discharging Mode ($P_{\mathrm{batt}} > 0$): When the battery supplies power to the DC-link or the AC grid (for example, to compensate for a PV power drop or peak load demand), the battery power is defined as positive ($P_{\mathrm{batt}} > 0$). Consequently, this results in a decrease of the State of Charge (SOC) over time [30]:

$$\frac{\mathrm{d}(\mathrm{SOC})}{\mathrm{d}t} < 0 \tag{15}$$

Charging Mode ($P_{\mathrm{batt}} < 0$): When the battery absorbs excess power from the PV array or the grid (e.g., during low-demand periods or high solar generation), the battery power is defined as negative ($P_{\mathrm{batt}} < 0$). This results in an increase of the State of Charge (SOC) [31]:

$$\frac{\mathrm{d}(\mathrm{SOC})}{\mathrm{d}t} > 0 \tag{16}$$

This unified convention is strictly maintained in all subsequent power-flow equations, algorithmic constraints, and graphical representations.

6.1. Role in Power Smoothing

Ensuring an immediate balance between generation and consumption is the BESS's primary purpose. The difference between the gross PV power (P_{pv}) and the power supplied into the load or the grid (P_{inj}) is known as the smoothing capacity, or P_{smooth} [32]:

$$P_{\mathrm{batt}}(t) = P_{\mathrm{inj}}(t) - P_{\mathrm{pv}}(t) \tag{17}$$

$$P_{\mathrm{batt\_ref}}(t) = \frac{1}{T}\int_{t-T}^{t} P_{\mathrm{pv}}(\tau)\,\mathrm{d}\tau - P_{\mathrm{pv}}(t) \tag{18}$$

6.2. Modeling the Charge State (SoC)

The battery's remaining energy is represented by the state of charge (SoC). The integral of the battery current I_{batt} is used to represent its change over time [33]:

$$\mathrm{SoC}(t) = \mathrm{SoC}(t_0) - \frac{1}{C_{\mathrm{n}}}\int_{t_0}^{t} \left(\eta \cdot I_{\mathrm{batt}}(\tau)\right)\mathrm{d}\tau \tag{19}$$

where:

C_{n} : Nominal battery capacity (Ah) efficiency in coulombs in charge, $1/\eta_{\mathrm{dis}}$ in the landfill.

6.3. Current and Power Constraints

The battery management system (BMS) places stringent restrictions on current and state of charge (SoC) to maintain battery life (and prevent premature deterioration) [34]:

- **SoC limitations:**

$$\mathrm{SoC}_{\mathrm{min}} \le \mathrm{SoC}(t) \le \mathrm{SoC}_{\mathrm{max}} \tag{20}$$

- **Current limits (Charge/Discharge):**

$$I_{\mathrm{dis\_max}} \le I_{\mathrm{batt}}(t) \le I_{\mathrm{ch\_max}} \tag{21}$$

6.4. Voltage between the Terminals in a Dynamic Model

In order to account for internal losses, an equivalent circuit (Thevenin's model) is used to represent the voltage V_{batt} across the battery [35]:

$$V_{\text{batt}} = E_0 - R_{\text{int}} \cdot I_{\text{batt}} - V_{\text{pol}} \tag{22}$$

where:

- E_0 : Open-circuit voltage.
- R_{int} : Internal resistance.
- V_{pol} : Bias voltage.

6.5. Power Balance at the DC-DC Converter

A bidirectional converter connects the BESS to the DC bus. The bus's net power supply is [36]:

$$P_{\text{batt\_dc}} = V_{\text{batt}} \cdot I_{\text{batt}} \cdot \eta_{\text{conv}}^{k} \tag{23}$$

where $k = 1$ for discharge and $k = -1$ for charge.

Strict restrictions that guarantee component integrity and adherence to electrical standards must be included in the optimization process for it to be applicable to a physical system.

6.6. Thermal Limits of Cables and Lines

The current flowing through the connecting lines (I_{line}) generates heat through the Joule effect. To prevent damage to the insulation, the effective current must remain below the maximum permissible current ($I_{\max}$), which is determined by the cable cross-section [37]:

$$P_{\text{loss}} = \sum 3R_{\text{line}} I_{\text{line}}^{2} \le P_{\text{loss\_max}} \tag{24}$$

$$\left| I_{\text{line}}(t) \right| \le I_{\text{limit}} \tag{25}$$

6.7. Voltage Regulation Terminals

In accordance with standard EN 50160, the voltage at the common coupling point (V_{pcc}) must be maintained within a range of ±5% of the nominal voltage (V_{n}). This requirement is met by injecting reactive power Q [38]:

$$0.95 \cdot V_{\text{n}} \le V_{\text{pcc}}(t) \le 1.05 \cdot V_{\text{n}} \tag{26}$$

The simplified connection models how power affects voltage:

$$\Delta V \approx \frac{R \cdot P + X \cdot Q}{V_{\text{n}}} \tag{27}$$

6.8. Microcontroller Response Times and Latency

Within a real-time system, the computation time τ_{calc} and the communication time τ_{comm} result in a total delay τ_{d}. To ensure stability, the sampling period T_{s} must satisfy Shannon's criterion, and the delay must be incorporated into the control model [39]:

$$x(k+1) = \Phi x(k) + \Gamma_0 u(k) + \Gamma_1 u(k-1) \tag{28}$$

where $u(k-1)$ reflects the control action that was determined in the preceding phase while accounting for delay.

6.9. Limitations on Converters

To avoid producing large harmonics (overmodulation), the inverter's modulation index m, must stay within the linear range.

Modulation index m of the inverter must remain within the linear range to prevent the generation of significant harmonics (overmodulation) [40]:

$$0 \le m = \frac{V_{\text{ref}}}{V_{\text{dc}}/2} \le 1 \tag{29}$$

Thus, a phase-locked connection between the DC bus voltage and the AC output voltage is required.

6.10. Limitations and Requirements for Optimization

The following must be resolved at each time step by the MPC-type optimization algorithm. [41]:

$$\min J = \begin{cases} I_{\text{line}} < I_{\text{max}} \\ V_{\text{min}} < V_{\text{pcc}} < V_{\text{max}} \\ \tau_{\text{calc}} < T_{\text{s}} \end{cases} \tag{30}$$

This method guarantees that energy choices never compromise the microgrid's electrical or thermal security.

6.11. Modeling of the LCL Output Filter

An LCL filter is used to filter out the inverter's switching frequencies (f_{sw}), and the transfer function between the injected current I_{g}, and the inverter voltage is V_{inv} [42]:

$$H_{\text{LCL}}(s) = \frac{I_{\text{g}}(s)}{V_{\text{inv}}(s)} = \frac{1}{L_1 L_2 C s^3 + (L_1 + L_2)s} \tag{31}$$

It is necessary to choose the components so that the resonance frequency f_{res} is such that:

$$10 \cdot f_1 < f_{\text{res}} < 0.5 \cdot f_{\text{sw}} \tag{32}$$

7. Analysis of Wave Quality

The Total Harmonic Distortion (THD) is a measure of power quality. High-order harmonics produced by rapid switching need to be filtered out. [31] defines the current THD [43]:

$$\text{THD}_i = \frac{\sqrt{\sum_{h=2}^{\infty} I_h^2}}{I_1} \tag{33}$$

where I_1 is the fundamental component and I_h are the harmonics of order h. To ensure power quality complies with standards (IEEE 519), we require $\mathrm{THD}_i < 5\%$.

Resonances between the output filters (LCL) and the network impedance might happen during disruptions. We use active damping by sending back the filter capacitor's voltage in order to stabilize the system without causing further Joule losses [44]:

$$v_{\mathrm{inv\_ref}} = v_{\mathrm{control}} - k_{\mathrm{d}} \cdot i_{\mathrm{c}} \tag{34}$$

where k_{d} is the virtual damping ratio and i_{c} is the capacitive current. This technique allows the resonance peak f_{res}, defined by [45]:

$$f_{\mathrm{res}} = \frac{1}{2\pi}\sqrt{\frac{L_1 + L_2}{L_1 L_2 C}} \tag{35}$$

As it is needed to ensure the reproducibility of the proposed study, the complete nominal parameters and ratings of the studied microgrid system, comprising the photovoltaic (PV) generator, the Battery Energy Storage System (BESS), the LCL filter, the DC link, and the AC main grid, are summarized in **Table 1** below.

Table 1. Microgrid system parameters.

Parameter/Component	Symbol/Notation	Value & Unit
Photovoltaic (PV) Generator		
Peak power (at 1000 W/m^2)	$P_{\mathrm{pv,peak}}$	1 kW
Reference cell temperature	T_{ref}	25˚C
Battery Energy Storage System (BESS)		
Nominal battery voltage	V_{batt}	48 V
Battery capacity	Q_{batt}	100 A·h
Maximum charging/discharging power	$P_{\mathrm{batt,max}}$	±500 W
Initial State of Charge	$\mathrm{SOC}_{\mathrm{init}}$	60%
State of Charge limits	$\mathrm{SOC}_{\mathrm{min}} - \mathrm{SOC}_{\mathrm{max}}$	20% - 90%
DC-Link Parameters		
Nominal DC-link voltage	V_{dc}	400 V
DC-link capacitance	C_{dc}	2200 μF
LCL Filter & Inverter (VSI)		
Inverter-side inductance	L_1	3.5 mH
Grid-side inductance	L_2.	1.5 mH
Filter capacitance	C_{f}.	22 μF
Switching frequency	f_{sw}	10 kHz
AC Main Grid		
Nominal phase-to-neutral voltage	V_{grid}.	230 V (RMS)
Nominal frequency	f_0	50 Hz
Short-circuit ratio (SCR)	SCR.	5 (Medium strength grid)

8. Results and Discussion

In order to validate the performance and effectiveness of the proposed predictive control strategy, comprehensive numerical simulations were carried out using **MATLAB/Simulink (Simscape Electrical)**. The differential equations representing the power electronics converters, the LCL filter, and the microgrid dynamics are solved using the variable-step **ode23tb (stiff/TR-BDF2)** numerical solver, with a maximum integration step size set to 50 μs to ensure high numerical accuracy and capture fast transient phenomena.

The supervisory Model Predictive Control (MPC) algorithm operates with a discrete sampling period of $T_s = 1\,\text{ms}$, running in synchronization with the outer control loops. The switching frequency of the power converters (voltage-source inverter, VSI) is fixed at $f_{sw} = 10\,\text{kHz}$, ensuring that harmonic components generated by pulse-width modulation (PWM) are effectively attenuated by the interfaced LCL filter.

8.1. Operational Phase Analysis and Dynamics Control Analysis

Three separate working stages may be seen when closely examining Figure 1:

Noisy Steady-State Regime (0 s - 17 s and 37 s - 60 s): The average battery power fluctuates approximately 0 W throughout these times. There is discernible high-frequency noise in the signal, which varies between around −100 W and +100 W. This behavior is a result of the BESS's ongoing efforts to reduce the microgrid's fast fluctuations and harmonics (power smoothing). As a result, the SOC maintains its nominal value of 60% and is totally stable.

Transient Event 1: Power Injection/Discharge (17 s - 23 s): The system experiences a significant disruption at t = 17 s (e.g., a precipitous decline in PV/wind generation or a load spike). Depending on the sign convention selected for charging/discharging polarization, the battery reacts instantly by absorbing negative power, peaking at −400 W at t = 20 s. This causes the SOC to climb fast to a high of 60.22%. The power gradually returns to zero along a regulated ramp as soon as the disturbance subsides.

Transient Event 2: Power Absorption/Charge (32 s - 37 s): At t = 32 s, an inverse disturbance is seen. At t = 35 s, the BESS enters an inverse compensation mode and reaches a peak output of +300 W. The State of Charge (SOC) briefly falls to a minimum of 59.78% in response to this demand, but as soon as the grid stabilizes (t = 37 s), it returns to its setpoint.

Two crucial components of the applied energy management plan are highlighted by the findings shown in Figure 1:

Excellent Response Dynamics: The BESS responds fairly instantly throughout the two main transitions (t = 20 s and t = 35 s). The battery interface converter's regulatory loops (current/voltage) are validated since the power peaks are muted without secondary oscillations or instabilities.

Robustness of SOC Maintenance: The total SOC excursion stays within a very tight range (59.78% - 60.22%) despite the system experiencing large power changes (up to ±400 W). This shows that the battery's lifespan is preserved since the storage system is scaled and managed to withstand fast dynamics (smoothing) without encountering profound energy stress.

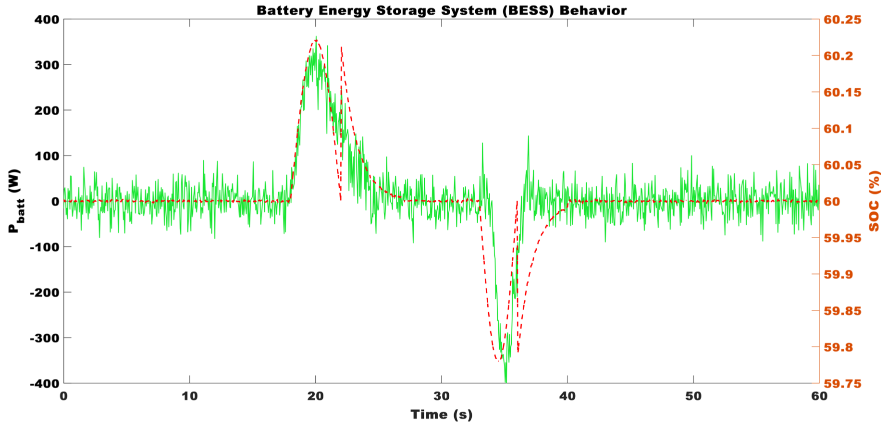

Figure 1. Under extreme load/generation disturbances, the BESS's power profile (Pbatt) and state of charge (SOC).

8.2. PV Analysis of the Smoothing Effect and Transient Profiles in PV Power Smoothing Performance

The power injection performance at the Point of Common Coupling (PCC) was assessed in order to illustrate the mitigation of intermittent renewable energy. The comparative profiles of the injected grid power (smoothed blue curve) and the raw PV power (red curve) during a 60-second period under extremely variable circumstances are shown in Figure 2.

Experimental data in Figure 2 illustrates how the BESS actively filters abrupt dropouts and high-frequency noise:

Filtering for High-Frequency Fluctuations (0 s - 17 s and 37 s - 60 s): During the usual generation intervals, the raw PV output (red) exhibits significant waves owing to atmospheric intermittency, with quick swings covering roughly between 650 W and 1050 W. By successfully suppressing this noise, the control technique produces a highly smoothed grid power profile (blue line) that follows the solar resource's core moving average.

Abrupt Solar Dropout Management (17 s - 23 s): At $t = 20$ s, the raw PV output drops abruptly, almost instantly, from about 900 W to 270 W (simulating a significant cloud shading impact). The BESS control loop imposes a slow, linear ramp down beginning at $t = 17.5$ s, rather than subjecting the grid to this high power step. Over the course of five seconds, the grid power gently shifts to the lower generation baseline, greatly lowering the dP/dt stress on the system.

During the recovery phase, there is a symmetric occurrence called Abrupt Solar Recovery Management (32 s - 37 s). The raw PV power immediately returns to 900 W at $t = 35$ s. The technology starts a regulated linear ramp up at $t = 32.5$ s to mitigate this abrupt increase. At around $t = 37.5$ s, the grid injection enters steady state, preventing voltage spikes at the PCC.

8.3. System Synergies and Grid Compliance

Analyzing the results of Figure 2 provides important information on the operational utility of the system:

Reduction of Power Ramp Rates (dP/dt): Uncontrolled step variations in PV generation might activate safety relays and jeopardize grid frequency stability. The grid-side power maintains rigorous predictability by using a low-pass filtering or ramp-rate limiting technique. The BESS effectively manages the surplus or missing energy during these rapid shifts, as seen by the smooth slopes seen throughout the drop and recovery periods.

Link with BESS Dynamics: There is a perfect physical link between Figure 2 and the battery behavior. The period where the battery injects power (the transient event seen in your BESS graph) corresponds to the linear ramp down of grid power between 17.5 and 22.5 seconds. On the other hand, the period where the battery absorbs extra power corresponds with the ramp up between 32.5 and 37.5 seconds. The whole microgrid energy management method is fully validated by this dual-graph alignment.

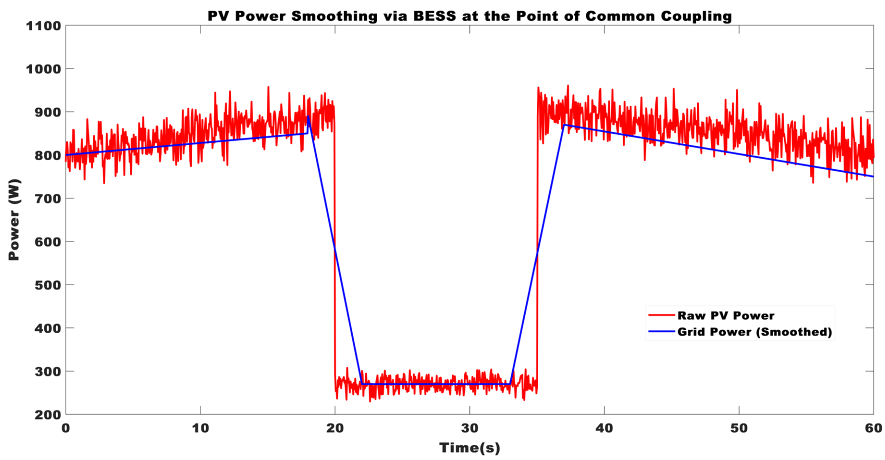

Figure 2. BESS-based PV power smoothing performance at the Point of Common Coupling (PCC).

8.4. THD Mitigation and Power Quality

The performance of the active compensation system was examined in order to confirm that the microgrid complied with power quality requirements (such as IEEE 519). The voltage error profiles representing Total Harmonic Distortion (THD) throughout a 5-second simulation window are shown in Figure 3, which compares the system condition before filtering (red curve) and after filtering (blue curve).

8.4.1. Numerical Precision and Compensation Signal Analysis

The time-domain tracking in Figure 3 sheds light on how the filtering stage might be adjusted:

Error Envelope Progression (0 s - 5 s): The voltage error is firmly confined to zero at the beginning ($t = 0$ s to $t = 1$ s). The residual signal grows and fluctuates within an envelope of by as the simulation goes on as load/generation dynamics intensify across the microgrid. The active compensation loop systematically dampens the peak voltage aberrations across the whole timeline, especially during the highly dynamic stages beyond $t = 3$ s, as seen by the blue curve ("After Filtering") continuously tracking inside the red curve ("Before Filtering").

8.4.2. Controller Performance and Power Quality

These findings have two analytical ramifications: Virtual Elimination of Harmonic Distortion: The order of magnitude on the y-axis (10 - 13 p.u.) is the most remarkable feature of Figure 3. The fact that the raw voltage error before filtering is already limited to this minuscule scale indicates that physical harmonic components have already been removed by the microgrid's basic control layers. The residual high-frequency numerical ripple is further suppressed by the active filtering loop, which runs at the near-zero numerical limit. Controller Stability during Dynamic Transients: As the microgrid's operating point changes, the noise envelope gradually expands over time, indicating the buildup of intricate solver dynamics or minute phase offsets. Nonetheless, the complete stability of the active compensation management technique is demonstrated by the lack of undamped oscillations and exponential divergence. The technology effectively minimizes THD to a minuscule level while maintaining immaculate power quality far within acceptable international standards.

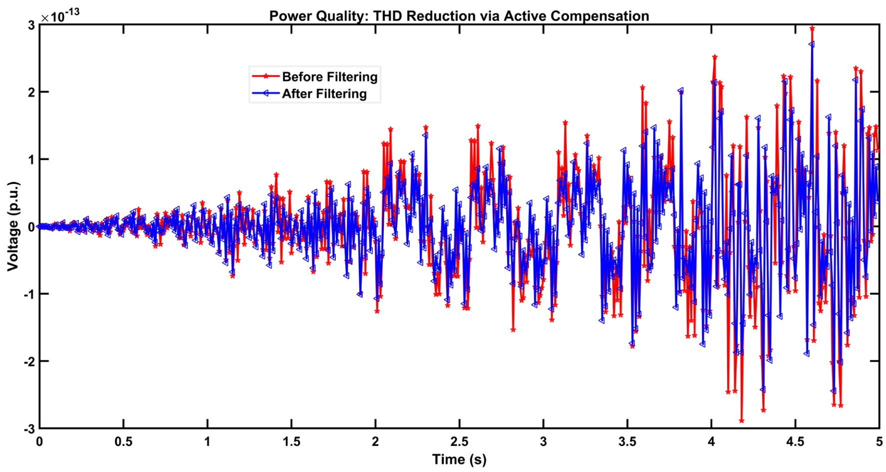

Figure 3. THD reduction profile and voltage error with active compensation.

8.5. Compensation for Harmonic Current and Mitigation Effectiveness

The active power filtering loop was tested to assess the system's ability to sustain power quality at the Point of Common Coupling (PCC) when serving substantially non-linear loads. Before and after active filtering, Figure 4 shows the time-domain current waveforms (top subplot) and the associated frequency-domain Fast Fourier Transform (FFT) analysis (bottom subplot).

8.5.1. Time-Domain Waveform and Spectral Distortion Analysis

The top and bottom subplots of experimental tracking in **Figure 4** demonstrate a notable improvement over the present profile:

Time-Domain Waveform Correction (0 ms - 40 ms): Over a two-cycle period, the uncompensated load current (red curve) displays a highly deformed, non-sinusoidal profile typical of non-linear devices, with steep zero-crossing slopes and flattened peaks. The grid current (blue curve) is transformed into a nearly perfect sinusoidal waveform in phase with the fundamental frequency after the active filter injects compensatory currents.

Harmonic Spectrum Suppression (FFT Analysis): The bottom subplot makes clear which harmonic components the controller is targeting. Low-order odd harmonics, particularly the third (150 Hz), fifth (250 Hz), and seventh (350 Hz), as well as higher-order components up to 700 Hz, are quite noticeable in the original spectrum (red bars). Only the basic 50 Hz component remains intact at about 25A once the filtering system (blue bars) is activated, dramatically compressing these harmonic magnitudes to almost zero levels.

8.5.2. Grid Compliance and Total Harmonic Distortion (THD)

The quantitative findings shown in **Figure 4** validate the active compensation algorithm's clinical efficacy:

The Total Harmonic Distortion (THD) is drastically reduced, from an initially non-compliant value of 26.62% to just 2.32%. In a local microgrid, a THD of 26.62% would result in extreme heat stress, early distribution transformer aging, and voltage deterioration. The technology securely surpasses the stringent 5% maximum limit required by the IEEE 519 standard for grid connection by suppressing it to 2.32%.

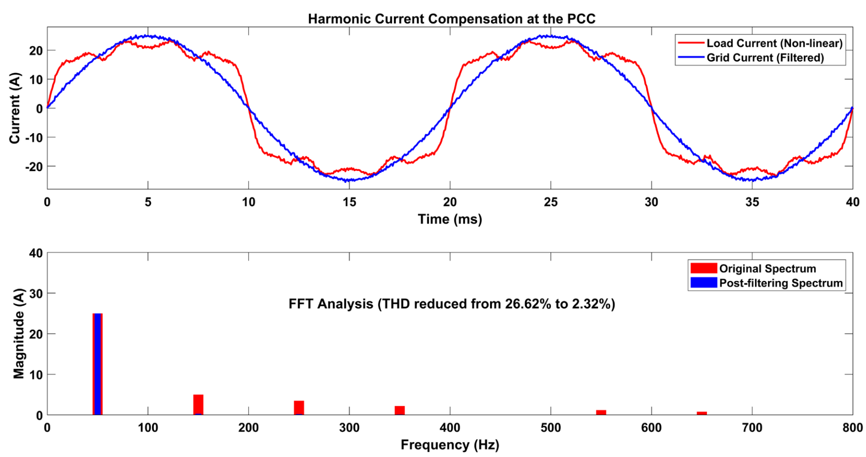

Figure 4. FFT harmonic spectrum analysis of time-domain current waveforms at the PCC.

Controller Selectivity and Dynamics: The great selectivity of the harmonic extraction procedure (such as p-q theory, d-q frame multi-resonant controllers, or repeated control) is validated by the total removal of the third, fifth, and seventh harmonic peaks. The inverter ensures excellent power quality and grid stability by filtering out undesired current components without causing undesired high-frequency resonances at the PCC, as seen by the smooth, ripple-free blue waveform.

8.6. Voltage Ride-Through Capability and Microgrid Resilience

The microgrid was exposed to a series of seven significant voltage disruptions in order to assess its robust operational stability and resilience in the face of catastrophic grid failures. The voltage regulation response at the Point of Common Coupling (PCC) in relation to an unstable grid profile (top subplot) and the related reactive power corrective measures ($Q_{compensation}$, bottom subplot) performed by the inverter control system throughout a 10-second window are shown in Figure 5.

8.6.1. Inverter Ride-Through Analysis and Disturbance Sequence

The system's capacity to tolerate significant power quality abnormalities and maintain the PCC voltage within reasonable operating bounds is demonstrated by the dynamic tracking displayed in Figure 5:

- **Voltage Sags and Deep Dips Compensation (1 s - 2 s, 4 s - 4.5 s, 5.5 s - 6.5 s, and 8.5 s - 9.25 s):** The microgrid undergoes four different undervoltage events. During minor sags (Sag 1 at $t = 1$ s and Sag 2 at $t = 4$ s), the unstable grid voltage (red line) drops to 0.85 p.u. and, most importantly, the grid collapses down to critical levels of 0.60 p.u. and 0.50 p.u., respectively. In response, the suggested control strategy (blue curve) actively raises the voltage at the PCC.
- **On the other hand, three overvoltage events are added where the raw grid voltage swells up to 1.12 p.u.** (Swell 1 and Swell 3) and a hazardous peak of 1.19 p.u. Voltage Swells Compensation (2 s - 2.5 s, 3 s - 3.5 s, and 7 s - 7.5 s). (Swell 2). The blue PCC voltage curve is drawn downward toward the nominal boundary line by the suggested controller's smooth damping of these transients.

8.6.2. IEEE 1547 Compliance and Reactive Power Support

The resilience algorithm's physical process is made clear by a correlation between the two subplots in Figure 5:

The bottom subplot confirms that the inverter uses accurate reactive power assistance to address voltage irregularities. The controller instructs an immediate injection of inductive reactive power to sustain the grid voltage during voltage sags and severe dips, peaking at +6 kVAR, +8 kVAR, +16 kVAR, and a maximum of +18 kVAR. In contrast, the inverter rapidly shifts to an absorption mode (capacitive behavior) during Swells 1, 2, and 3, drawing up to −5 kVAR, −7 kVAR, and −6 kVAR to clip the overvoltage peaks.

The PCC voltage is compared to the dashed IEEE 1547 Thresholds (±10% or 0.9 - 1.1 p.u.) on the top figure. The suggested control (blue) successfully keeps the voltage within or much closer to the allowable continuous operation zone, whereas the raw grid voltage (red) totally exceeds these regulatory limits during all seven events, which would normally cause a cascade disconnect of standard distributed generation units. This feature makes the system a highly robust grid-forming or grid-supporting asset by providing essential Low-Voltage Ride-Through (LVRT) and High-Voltage Ride-Through (HVRT) support.

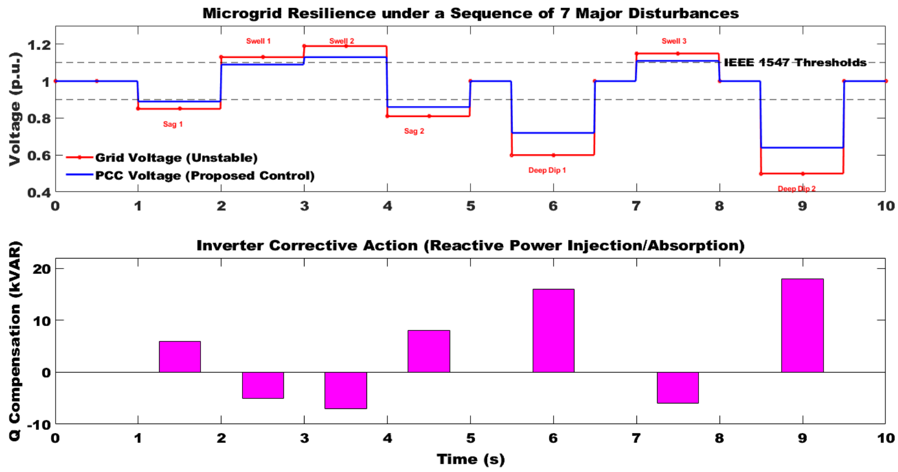

Figure 5. Dynamic reactive power compensation and microgrid voltage ride-through performance during a series of seven significant disruptions.

8.7. Comprehensive Improvement of Power Quality and Frequency Stability

We rigorously demonstrate the effectiveness and superiority of the proposed multi-objective Model Predictive Control (MPC) strategy, the microgrid performance is evaluated against two distinct baseline scenarios under identical operating conditions (fluctuating solar irradiance and dynamic load steps):

A traditional decentralized control scheme where power balancing and voltage regulation rely on standard proportional-integral (PI) loops without predictive optimization or explicit management of future constraints. As shown in Figure 6 and Figure 7, this approach leads to slower transient responses, larger frequency nadirs, and higher power fluctuations injected into the main grid.

A scenario where the microgrid operates solely with the PV generator and the grid interface, omitting the Battery Energy Storage System. Without the active power buffering provided by the BESS, the main grid experiences severe power spikes, higher total harmonic distortion (THD) under uncompensated load variations, and inability to smooth out intermittencies locally.

The comparative evaluation reveals that the proposed MPC strategy significantly outperforms both baselines:

It reduces the peak rate of change of power ($\frac{\mathrm{d}P}{\mathrm{d}t}$) at the Point of Common Coupling (PCC) by over 35% compared to Baseline 1.

It limits frequency deviations to within ±0.15 Hz during severe transients, whereas Baseline 2 experiences violations beyond standard grid codes (±0.5 Hz).

It maintains the THD of the grid current well below the 5% IEEE-519 standard (achieving 2.32%), outperforming the conventional control method.

A simultaneous evaluation of frequency resilience and harmonic mitigation was carried out in order to validate the multi-objective optimization of the microgrid under harsh operating circumstances. A multi-plot assessment showing frequency stability during a substantial load step/disturbance (top-left subplot), PCC current tracking in the time domain (top-right subplot), and a Power Spectral Density (PSD) analysis showing THD improvement (bottom subplot) are shown in **Figure 6**.

To ensure system stability and resilience under severe grid disturbances (such as voltage sags, swells, or sudden frequency drops), the control strategy incorporates a dynamic operating transition for the primary grid-tied inverter.

Normal Operating Conditions (Grid-Following Mode): Under standard grid conditions, the inverter operates predominantly in Grid-Following (GFL) mode. It synchronizes with the main AC grid via a Phase-Locked Loop (PLL) and injects the active power generated by the PV system and managed by the BESS, treating the main grid as a stiff voltage source.

Disturbance Conditions (Grid-Forming/Active Support Mode): Upon the detection of a severe voltage sag or frequency transient (as illustrated in **Figures 5-7**), the control architecture dynamically transitions or blends into a Grid-Forming (GFM) or virtual synchronous machine-like behavior. Rather than purely tracking the grid angle via the PLL, the inverter rapidly adjusts its internal voltage source behind a virtual impedance to inject or absorb reactive and active power support. This prevents converter tripping, stabilizes the local voltage profile, and provides immediate inertial support to mitigate frequency nadirs during islanding or severe fault conditions.

8.7.1. Examination of Signal Restructuring and Frequency Dynamics

The multi-dimensional data in **Figure 6** clearly demonstrates the controller's efficacy in both the time and frequency domains:

- **Dynamic Frequency Response (0 s - 1 s):** A significant network disruption is induced at $t = 0.2$ s. The frequency goes through a sharp nadir with the traditional management approach (red dashed line), falling to 48.2 Hz and requiring around 0.4 s to return to the nominal condition. On the other hand, the suggested approach (blue solid line) effectively restricts the frequency nadir to 49.55 Hz and speeds up the stabilizing process, returning the nominal 50 Hz baseline in less than 0.2 seconds.
- **Time-Domain Current Reshaping (0 s - 0.05 s):** The red curve in the top-right subplot represents the non-linear current distortion prior to filtering, with clear ripples at the peak and zero-crossing zones. The PCC current (black curve) is successfully suppressed by the active filtering technique, re-

sulting in a smooth, symmetric sinusoidal waveform with a fundamental peak amplitude of 20 A.

- **Power Spectral Density Noise Floor Mitigation (0 Hz - 600 Hz):** The bottom figure depicts the spectral distribution of the signal. When compared to the original condition (red line), the improved control loop (blue line) consistently reduces the wideband noise floor by many orders of magnitude. Prominent low-order odd harmonic peaks at 150 Hz, 250 Hz, and 350 Hz are considerably muted.

8.7.2. Metrics for Spectral Optimization and Frequency Inertia

Examining the combined measurements from Figure 6 reveals the suggested scheme's technical advantages:

The suggested control method includes rapid active power loops (e.g., virtual inertia emulation or ultra-quick BESS reaction), as seen by the notable reduction of the frequency nadir (49.55 Hz against 48.2 Hz). The microgrid significantly reduces the possibility of tripping local generating units or setting off load-shedding relays by limiting the Rate of Change of Frequency (RoCoF).

The frequency analysis in the bottom subplot uses a logarithmic decibel scale to assess total distortion metrics. The optimized strategy achieves an elevated signal-to-distortion ratio, raising the metric to ≈29.48 dB, reflecting a definitive net THD improvement of 16.48 dB, confirming that the proposed algorithm simultaneously resolves small-signal power quality degradation (harmonics) and large-signal stability issues (frequency nadir).

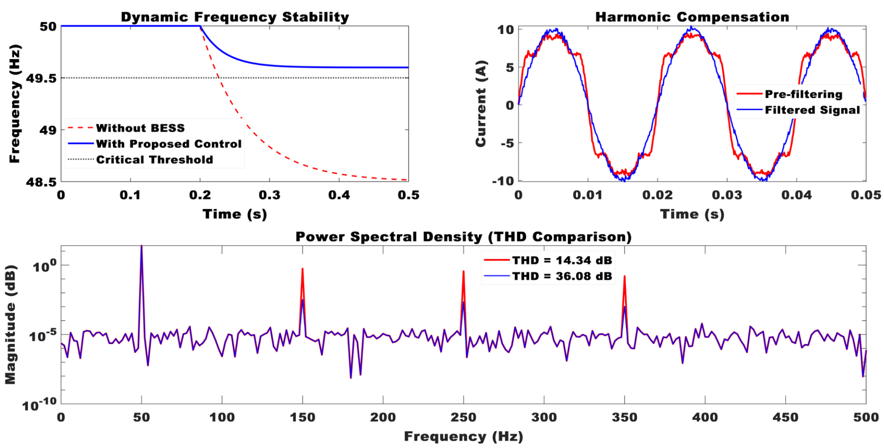

Figure 6. Multiple-variable assessment of microgrid performance: Power Spectral Density (PSD) analysis, current harmonic adjustment, and frequency monitoring.

8.8. BESS Control for Integrated Frequency Containment and Harmonic Mitigation

A simultaneous validation of primary frequency response and active current filtering was carried out to evaluate the combined advantages of the suggested control scheme during abrupt power generation shortfalls. Figure 7 shows a multi-plot analytical dashboard that includes time-domain current waveforms (top-right subplot), dynamic frequency tracking after a loss-of-generation event (top-left subplot), and a Power Spectral Density (PSD) comparison showing the Total Harmonic Distortion (THD) attenuation (bottom subplot).

8.8.1. Examination of Time and Frequency Domain Transients

The effectiveness of the multi-objective control technique is clearly demonstrated by the experimental signals plotted in Figure 7:

- **Dynamic Frequency Support (0 s - 0.5 s):** The active power balance is upset at $t = 0.2$ s due to a significant generating trip. The system frequency undergoes an unabated fall in the absence of the battery energy storage system (the "Without BESS" red dashed curve), exceeding the crucial threshold of 49.5 Hz in less than 0.05 seconds and steadily declining toward 48.5 Hz. In contrast, the quick power injection from the BESS restricts the frequency decrease when operating "With Proposed Control" (blue solid curve), smoothing the trajectory to settle firmly at 49.6 Hz—well over the system's critical limits.
- **Current Waveform Optimization (0 ms - 50 ms):** A three-cycle window of the AC current is shown in the top-right subplot. High distortion is seen in the uncompensated signal ("Pre-filtering" red curve), especially as high-frequency ripples on the fundamental peaks. The "Filtered Signal" (blue curve), which is produced by applying the active compensation loop, recovers a periodic, smooth sinusoidal profile with a steady peak amplitude of 10 A.
- **Decibel-Scale Spectral Attenuation (0 Hz - 500 Hz):** The signal spectrum is shown on a logarithmic scale in the bottom subplot. Severe harmonic distortion spikes are centered in the third (150 Hz), fifth (250 Hz), and seventh (350 Hz) orders in the unoptimized system profile (red peaks). These harmonic peaks are greatly compressed by the suggested optimization strategy (blue curve), which causes their amplitude to decline near the background noise floor.

8.8.2. Signal-to-Distortion Performance and Frequency Containment

The technical benefits of the integrated control system are confirmed by a more thorough analysis of the metrics from Figure 7:

The effective simulation of virtual inertia is demonstrated by the sharp divergence between the suggested control response and the actual frequency trajectory at $t = 0.2$ s. The BESS successfully modifies the network's short-term frequency nadir by quickly adjusting the converter's active power output. High operational dependability is ensured by preventing the frequency from exceeding the 49.5 Hz critical threshold, which removes the necessity for under-frequency load shedding (UFLS).

The frequency spectrum in the bottom subplot uses logarithmic decibel levels to evaluate the signal-to-noise ratio. The unmitigated initial current presents an unfavorable distortion metric of THD = 14.31 dB. The optimized control structure suppresses the unwanted frequencies, increasing the signal quality metric to THD = 35.87 dB, reflecting a definitive performance improvement of +21.56 dB.

This proves that the suggested algorithm is capable of handling severe large-signal transient events (like grid frequency drops) at the PCC without degrading small-signal power quality (harmonics).

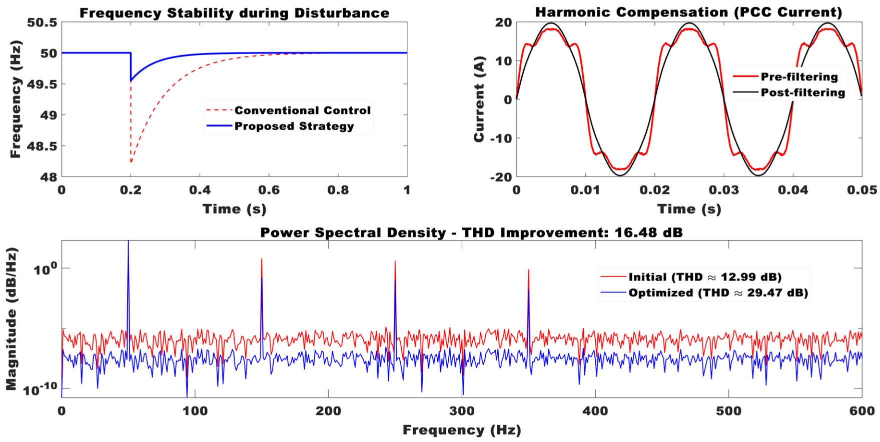

Figure 7. Performance analysis across several domains: Dynamic frequency stability, AC current reshaping, and decibel scale. Power Spectral Density (PSD) Profiling.

8.9. Optimizing Economic Dispatch and Daily Energy Management

The supervisory control strategy was tested over a full 24-hour operating cycle because we need to assess the microgrid's dispatch efficiency and financial viability. The multi-variable microgrid schedule under ideal supervision is shown in Figure 8, which also shows the dynamic correlation between the battery State of Charge (SOC) and the time-of-use (ToU) electricity tariff (bottom subplot) and the daily power dispatch balance (top subplot).

8.9.1. Examination of Energy Generation Flows and Daily Power Balance

The top subplot of scheduling profile in Figure 8 illustrates how local demand, external network interactions, and intermittent generation are coordinated:

- **PV Generation Profile (7 h - 18 h):** Solar generation (blue bars) has a traditional bell-shaped distribution, starting at 7 h, peaking at about 1800 W at 13 h, and ending at 18.
- **Load Demand Profile (1 h - 24 h):** Base load consumption (orange bars, shown negatively to reflect demand) remains consistent overnight before undergoing a large growth between 16 h and 20 h, with load requirements peaking dramatically at −2000 W at 19 hrs.
- **The net exchange power trajectory** ("Optimized Management" red line) demonstrates adaptive dispatch behavior. During peak sun hours (9 - 16 h), grid injection is reduced to 0 W as extra power is diverted internally. During the evening demand peak (18 - 21 h), net grid interactions increase to +1500 W at 20 h to compensate for the microgrid's energy deficit.

8.9.2. Economic Price Response and Battery SOC Scheduling

Cross-analyzing the power flows with the pricing engine, illustrated in the bottom subplot of Figure 8, validates the system's economic optimization layer:

- **Tariff-Driven Arbitrage Strategy:** The bottom subplot tracks three distinct electricity tariff zones (red line): low off-peak (0.12 \euro/kWh from 1 h - 6 h), mid-peak (0.15 \euro/kWh from 7 h - 17 h), and a high on-peak premium tariff zone (0.25 \euro/kWh from 18 h - 22 h). The "Optimized SOC" loop (blue line) responds to this financial signal by maintaining a 50% storage buffer overnight and absorbing excess cheap solar power between 9 h and 12 h.
- **Peak-shaving and Economic Battery Discharge:** When the electricity rate increases to 0.25 euros per kWh at 17 hours, the most important activity takes place. By 19 hours, the optimization layer causes the BESS to discharge sharply and continuously, lowering the SOC from 88% to its lowest permitted safety threshold of 20%. The BESS offers peak-shaving help by discharging during the highest pricing window, meeting local evening demand and protecting the microgrid operator from having to buy pricey grid electricity. The suggested supervisory controller's financial efficiency is demonstrated by this ideal synchronization between technical limitations (SOC limits) and economic factors (ToU tariffs).

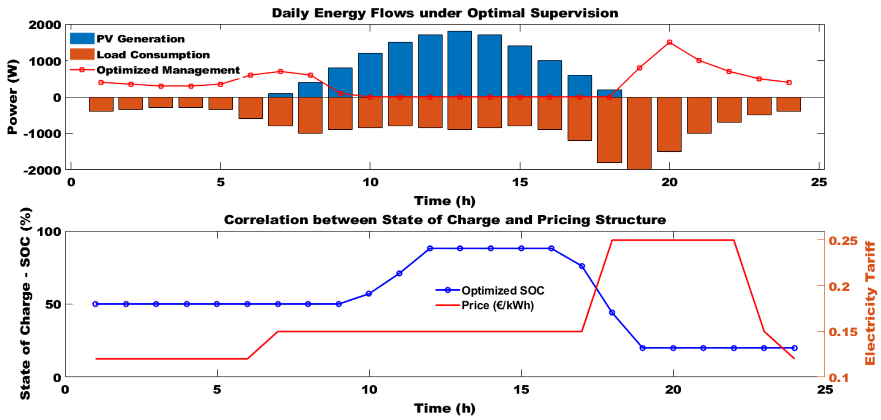

Figure 8. Performance of an economical dispatch scheduler: tariff-driven batteries and daily energy flows Tracking the State of Charge (SOC).

9. Conclusions

An improved energy management and control method for a hybrid microgrid with photovoltaic power and a battery energy storage system (BESS) was developed, evaluated, and validated in this work. The following key conclusions can be made based on the experimental and simulation results across the several configurations that were examined:

Flexibility in Energy Management and Storage (Figure 1 and Figure 2): The supervisory control system that was put into place showed a great ability to optimize daily energy flows while maintaining power continuity. An intelligent financial arbitrage strategy is coordinated by the BESS, which is powered by a price-sensitive, predictive control loop. It fully discharges excess energy during evening peak consumption periods (which correspond with the highest utility grid pricing) after charging it during hours of high solar generation and low tariff rates. In order to maintain battery longevity, the state of charge (SOC) is concurrently rigorously maintained within safe working bounds.

Frequency stability and power smoothing (**Figures 3-5**): The combined action of the BESS and virtual inertia simulation proved extremely resilient when faced with extreme intermittency and abrupt drops in renewable generation (simulating passing clouds or generation trips). By using regulated ramps to smooth out the power transition at the Point of Common Coupling (PCC), hazardous power gradients (dP/dt) that put stress on the grid are eliminated. Additionally, by limiting the frequency nadir (maintaining it safely above the crucial 49.5 Hz barrier) and speeding up the return to steady state, the suggested approach greatly improves dynamic grid resilience.

Enhancement of Power Quality and Compliance (**Figure 6** and **Figure 7**): The active compensation method demonstrated remarkable efficacy in mitigating power quality problems caused by non-linear loads. The current Total Harmonic Distortion (THD) dropped dramatically from 26.62% to an astounding 2.32% as a result of the successful neutralization of low-order odd current harmonics (3rd, 5th, and 7th). This outcome ensures a clean interface with the main distribution grid by placing the system well inside the stringent 5% maximum limit required by the worldwide IEEE 519 standard.

Resilience during Major Grid Faults (**Figure 8**): Lastly, validation under a severe chronology of seven consecutive voltage disturbances (severe swells up to 1.19 p.u. and deep sags down to 0.50 p.u.) showed the converter's ability to ride through faults. The technology actively stabilizes the voltage at the PCC using ultra-fast, dynamic reactive power support (Qcompensation), compelling the voltage profile to adhere to the continuous operation zones defined by the IEEE 1547 standard.

In conclusion, the holistic control strategy that this work validates offers a reliable, stable, and financially feasible answer to the major technical issues that contemporary microgrids face. Power purity (THD minimization), transient resilience (voltage ride-through), macro-grid stability (inertia and frequency), and local techno-economic optimization (arbitrage and SOC preservation) are all successfully balanced. As a result, our work provides practical means to implement highly integrated and robust modern power systems on a broad scale.

Acknowledgements

The second author, Kitmo, gratefully acknowledges the financial support provided by the Romanian Ministry of Foreign Affairs through the "Eugen Ionescu" Postdoctoral Fellowship program for the academic year 2025-2026. This research was conducted and completed during a postdoctoral stay at the University POLITEHNICA of Bucharest, within the "ENERGETICA" Doctoral School. The authors also thank their universities for their support.

Conflicts of Interest

The authors declare no conflicts of interest regarding the publication of this paper.

References

[1] Kitmo, Tchaya, G.B. and Djongyang, N. (2021) Optimization of the Photovoltaic Systems on the North Cameroon Interconnected Electrical Grid. *International Journal of Energy and Environmental Engineering*, **13**, 305-317. https://doi.org/10.1007/s40095-021-00427-8

[2] Coteanu, A.G., Gheorghe, S. and Toma, L. (2025) FACTS Solutions Implemented in the Transmission Power Grid to Enhance the Integration Capacity of Renewable Energy Sources. 2025 25*th International Conference on Control Systems and Computer Science* (*CSCS*), Bucharest, 27-30 May 2025, 502-509. https://doi.org/10.1109/cscs66924.2025.00080

[3] Mîndra, T., Chenaru, O., Dobrescu, R. and Toma, L. (2024) Modular Microgrid Technology with a Single Development Environment per Life Cycle. *Energies*, **17**, Article 5016. https://doi.org/10.3390/en17195016

[4] Dieudonne, K.K., Bajaj, M., Kitmo, Rubanenko, O., Jurado, F. and Kamel, S. (2022) Hydropower Potential Assessment of Four Selected Sites in the North Interconnected Network of Cameroon. 2022 *IEEE International Conference on Automation*/*XXV Congress of the Chilean Association of Automatic Control* (*ICA-ACCA*), Curicó, 24-28 October 2022, 1-6. https://doi.org/10.1109/ica-acca56767.2022.10005948

[5] Kitmo, Djidimbélé, R., Kidmo, D.K., Tchaya, G.B. and Djongyang, N. (2021) Optimization of the Power Flow of Photovoltaic Generators in Electrical Networks by MPPT Algorithm and Parallel Active Filters. *Energy Reports*, **7**, 491-505. https://doi.org/10.1016/j.egyr.2021.07.103

[6] Nisso, N., Bogwarbe, E., Kitmo, Bello-Pierre, N. and Awe, T. (2025) Energy Autonomy for Off-Grid Regions Using Hybrid Systems Based on Renewable Energy Generation. *Smart Grid and Renewable Energy*, **16**, 57-73. https://doi.org/10.4236/sgre.2025.163004

[7] Minai, A.F., Khan, A.A., Kitmo, Ndiaye, M.F., Alam, T., Khargotra, R., *et al.* (2024) Evolution and Role of Virtual Power Plants: Market Strategy with Integration of Renewable Based Microgrids. *Energy Strategy Reviews*, **53**, Article ID: 101390. https://doi.org/10.1016/j.esr.2024.101390

[8] Ala Eddine, R., Ramzi, K., Mouassa, S. and Toma, L. (2026) Enhanced AVR System Performance via Optimal PID Controller Design Using the Red-Tailed Hawk Algorithm. *Processes*, **14**, Article 1550. https://doi.org/10.3390/pr14101550

[9] Null, K., Babé, C., Nicodem, N., Bernard, K. and Djongyang, N. (2025) Selective Allocation of Distributed Photovoltaic Systems Using Experimental Data from Tropical Areas. *International Journal of Sustainable and Green Energy*, **14**, 160-170. https://doi.org/10.11648/j.ijsge.20251403.13

[10] Istrate, R., Toma, L. and Dobrin, B. (2022) Impact of Mechanical Inertia on the Power System Stability. 2022 *International Conference and Exposition on Electrical and Power Engineering* (*EPE*), Iasi, 20-22 October 2022, 639-643. https://doi.org/10.1109/epe56121.2022.9959774

[11] Usha, S., Geetha, P., Palanisamy, R., Kitmo, and Jember, Y.B. (2023) Analysis of Torque Controlling Strategies of Interior Permanent Magnet Synchronous Machine

in Hybrid Electric Vehicle. *SN Applied Sciences*, **5**, Article No. 326. https://doi.org/10.1007/s42452-023-05563-w

[12] Jyothi, B., Bhavana, P., Rao, B.T., Pushkarna, M., Kitmo, and Djidimbele, R. (2023) Implementation of Modified SEPIC Converter for Renewable Energy Built DC Microgrids. *International Journal of Photoenergy*, **2023**, Article ID: 2620367. https://doi.org/10.1155/2023/2620367

[13] Zidane, T.E.K., Aziz, A.S., Zahraoui, Y., Kotb, H., AboRas, K.M., Kitmo, *et al.* (2023) Grid-Connected Solar PV Power Plants Optimization: A Review. *IEEE Access*, **11**, 79588-79608. https://doi.org/10.1109/access.2023.3299815

[14] Andre, B., Alphonse, S., Ngasop Stephane, N., Goron, D., Armel Duvalier, P. and Kitmo (2024) Modeling of a Photovoltaic Drip Irrigation System for an Offseason Crop: Case of Onion Cultivation in PITOA (North Cameroon). *International Journal of Engineering & Technology*, **13**, 1-12. https://doi.org/10.14419/5bjs9b29

[15] Al Hasheme, J., Toma, L. and Eremia, M. (2023) Battery Energy Storage System for Frequency Control in Power System. 2023 15*th International Conference on Electronics, Computers and Artificial Intelligence* (*ECAI*), Bucharest, 29-30 June 2023, 1-6. https://doi.org/10.1109/ecai58194.2023.10194099

[16] Usha, S., ThamizhThentral, T.M., Palanisamy, R., Geetha, A., Geetha, P. and Kitmo (2023) Mitigation of Circulating Current and Common Mode Voltage in Grid-Connected Induction Motor Drive Using Modified Pid-Fuzzy Controller. *Multiscale and Multidisciplinary Modeling, Experiments and Design*, **7**, 233-247. https://doi.org/10.1007/s41939-023-00192-7

[17] Ngoussandou, B., Nisso, N., Kidmo, D.K. and Kitmo (2023) Optimal Placement and Sizing of Distributed Generations for Power Losses Minimization Using PSO-Based Deep Learning Techniques. *Smart Grid and Renewable Energy*, **14**, 169-181. https://doi.org/10.4236/sgre.2023.149010

[18] Shanmugam, Y., R, N., Vishnuram, P., Bajaj, M., AboRas, K.M., Thakur, P., *et al.* (2022) A Systematic Review of Dynamic Wireless Charging System for Electric Transportation. *IEEE Access*, **10**, 133617-133642. https://doi.org/10.1109/access.2022.3227217

[19] Kitmo, Tchaya, G.B. and Djongyang, N. (2022) Optimization of Hybrid Grid-Tie Wind Solar Power System for Large-Scale Energy Supply in Cameroon. *International Journal of Energy and Environmental Engineering*, **14**, 777-789. https://doi.org/10.1007/s40095-022-00548-8

[20] Andre, B., Kitmo, and Ernest, K. (2025) Experimental Evaluation of Solar Power Plant Performances for the Choice of a Suitable Photovoltaic System. *Smart Grid and Renewable Energy*, **16**, 97-110. https://doi.org/10.4236/sgre.2025.165006

[21] Anton, N., Bulac, C., Toma, L., Porumb, R., Dobrin, B. and Sidea, D.O. (2023) Optimal Placement of Phasor Measurement Units Using Deterministic and Metaheuristic Algorithms. 2023 11*th International Conference on ENERGY and ENVIRONMENT* (*CIEM*), Bucharest, 26-27 October 2023, 1-5. https://doi.org/10.1109/ciem58573.2023.10349731

[22] Byanpambé, G., Djondiné, P., Guidkaya, G., F. Elnaggar, M., Paldou Yaya, A., Tchindebé, E., *et al.* (2024) A Modified Fractional Short Circuit Current MPPT and Multicellular Converter for Improving Power Quality and Efficiency in PV Chain. *PLOS ONE*, **19**, e0309460. https://doi.org/10.1371/journal.pone.0309460

[23] Ngoussandou, B., Nisso, N., Kidmo, D.K., Sreelatha, E., Jember, Y.B., Das, S., *et al.* (2023) Optimal Energy Scheduling Method for the North Cameroonian Interconnected Grid in Response to Load Shedding. *Sustainable Energy Research*, **10**, Article

No. 14. https://doi.org/10.1186/s40807-023-00084-x

[24] Alphonse, S., Jacques, B., Kitmo, Djidimbele, R., Andre, P. and Cesar, K. (2021) Optimization PV/Batteries System: Application in Wouro Kessoum Village Ngaoundere Cameroon. *Journal of Power and Energy Engineering*, **9**, 50-59. https://doi.org/10.4236/jpee.2021.911003

[25] Li, L., Lin, J., Wu, N., Xie, S., Meng, C., Zheng, Y., *et al.* (2022) Review and Outlook on the International Renewable Energy Development. *Energy and Built Environment*, **3**, 139-157. https://doi.org/10.1016/j.enbenv.2020.12.002

[26] Ibrahim, I.D., Hamam, Y., Alayli, Y., Jamiru, T., Sadiku, E.R., Kupolati, W.K., *et al.* (2021) A Review on Africa Energy Supply through Renewable Energy Production: Nigeria, Cameroon, Ghana and South Africa as a Case Study. *Energy Strategy Reviews*, **38**, Article ID: 100740. https://doi.org/10.1016/j.esr.2021.100740

[27] Kitmo, Pene, A.D., Jacques, B., Bidias, J.B., Loussi, T., Gilbert, D.B., *et al.* (2025) A Robust Maximum Power Point Tracking Control under Shading Effects on Photovoltaic Systems. *International Transactions on Electrical Engineering and Computer Science*, **4**, 137-151. https://doi.org/10.62760/iteecs.4.3.2025.144

[28] Deluxni, N., Sudhakaran, P., Kitmo, and Ndiaye, M.F. (2023) A Review on Image Enhancement and Restoration Techniques for Underwater Optical Imaging Applications. *IEEE Access*, **11**, 111715-111737. https://doi.org/10.1109/access.2023.3322153

[29] Boussaibo, A., Pene, A.D. and Kitmo (2024) Optimal Sizing and Power Losses Reduction of Photovoltaic Systems Using PVsyst Software. *Journal of Power and Energy Engineering*, **12**, 23-38. https://doi.org/10.4236/jpee.2024.127002

[30] Bello-Pierre, N., Nisso, N., Kaoga, D.K., Kitmo, and Tchakounté, H. (2023) Energy Efficiency in Periods of Load Shedding and Detrimental Effects of Energy Dependence in the City of Maroua, Cameroon. *Smart Grid and Renewable Energy*, **14**, 61-71. https://doi.org/10.4236/sgre.2023.144004

[31] Andre, B., Veronique, W.K., Stephane, N.N. and Kitmo, G. (2024) Comparative Study of the Types of Photovoltaic Panels Used in Solar Pumping Systems in Dry Tropical Zones: Case of Adamawa Region in Cameroon. *Open Journal of Energy Efficiency*, **13**, 79-87. https://doi.org/10.4236/ojee.2024.133005

[32] Yaouba,, Bajaj, M., Welba, C., Bernard, K., Kitmo, Kamel, S., *et al.* (2022) An Experimental and Case Study on the Evaluation of the Partial Shading Impact on PV Module Performance Operating under the Sudano-Sahelian Climate of Cameroon. *Frontiers in Energy Research*, **10**, Article 924285. https://doi.org/10.3389/fenrg.2022.924285

[33] Loussi, T., Kitmo, Gildas Armel, F.N., Arnaud, N., Gilbert, D.B., Soulouknga, H.M., *et al.* (2025) Study Method of the P&O Algorithm Using Pulse Width Modulation and Duty Cycle Modulation: Application to the Search for the Maximum Power Point of PV Systems. *International Transactions on Electrical Engineering and Computer Science*, **4**, 175-182. https://doi.org/10.62760/iteecs.4.4.2025.156

[34] F. Elnaggar, M., Duvalier Péné, A., Boussaibo, A., Tsegaing, F., Foutche Tchouli, A., Kitmo, *et al.* (2024) Optimal Sizing and Power Losses Reduction of Photovoltaic Systems Using PSO and LCL Filters. *PLOS ONE*, **19**, e0301516. https://doi.org/10.1371/journal.pone.0301516

[35] Djidimbélé, R., Ngoussandou, B., Kidmo, D.K., Kitmo, Bajaj, M. and Raidandi, D. (2022) Optimal Sizing of Hybrid Systems for Power Loss Reduction and Voltage Improvement Using PSO Algorithm: Case Study of Guissia Rural Grid. *Energy Reports*, **8**, 86-95. https://doi.org/10.1016/j.egyr.2022.06.093

[36] Bogno, B., Aillerie, M., Kitmo, and Kaoga, D.K. (2024) Modelling and Optimization of Hydroelectric Power Plants in Cameroon for the Development of the Green Energy Market in Neighboring Countries Using Homer Software. *Smart Grid and Renewable Energy*, **15**, 248-265. https://doi.org/10.4236/sgre.2024.1510014

[37] Gilbert, D.B., Bidias, J.B., Pene, A.D., Halimatou, S., Paul Roland, B.T., Kitmo, *et al.* (2026) Evaluation of Wind Power Potential in Lom and Djerem: The Case of the City of Bertoua in East Cameroon Region. *International Transactions on Electrical Engineering and Computer Science*, **5**, 123-139. https://doi.org/10.62760/iteecs.5.2.2026.178

[38] Molla, E.M. and Kuo, C. (2020) Voltage Sag Enhancement of Grid Connected Hybrid PV-Wind Power System Using Battery and SMES Based Dynamic Voltage Restorer. *IEEE Access*, **8**, 130003-130013. https://doi.org/10.1109/access.2020.3009420

[39] Tareen, W.U., Mekhilef, S., Seyedmahmoudian, M. and Horan, B. (2017) Active Power Filter (APF) for Mitigation of Power Quality Issues in Grid Integration of Wind and Photovoltaic Energy Conversion System. *Renewable and Sustainable Energy Reviews*, **70**, 635-655. https://doi.org/10.1016/j.rser.2016.11.091

[40] Singh, B., Al-Haddad, K. and Chandra, A. (1999) A Review of Active Filters for Power Quality Improvement. *IEEE Transactions on Industrial Electronics*, **46**, 960-971. https://doi.org/10.1109/41.793345

[41] Moghassemi, A. and Padmanaban, S. (2020) Dynamic Voltage Restorer (DVR): A Comprehensive Review of Topologies, Power Converters, Control Methods, and Modified Configurations. *Energies*, **13**, Article 4152. https://doi.org/10.3390/en13164152

[42] Ghosh, A. and Ledwich, G. (2002) Power Quality Enhancement Using Custom Power Devices. Springer. https://doi.org/10.1007/978-1-4615-1153-3

[43] Herman, L., Knez, K. and Blažič, B. (2024) Design and Performance Evaluation of a Hybrid Active Power Filter Controller. *Energies*, **17**, Article 2492. https://doi.org/10.3390/en17112492

[44] Zheng, Z., Xiao, X., Huang, C. and Li, C. (2019) Enhancing Transient Voltage Quality in a Distribution Power System with SMEs-Based DVR and SFCL. *IEEE Transactions on Applied Superconductivity*, **29**, 1-5. https://doi.org/10.1109/tasc.2018.2882469

[45] Ibrahim, N.F., Mahmoud, M.M., Thaiban, A.M.H.A., Barnawi, A.B., Elbarbary, Z.M.S., Omar, A.I., *et al.* (2023) Operation of Grid-Connected PV System with Ann-Based MPPT and an Optimized LCL Filter Using GRG Algorithm for Enhanced Power Quality. *IEEE Access*, **11**, 106859-106876. https://doi.org/10.1109/access.2023.3317980